# Reduction of mine suspected areas by multisensor airborne measurements – first results

Martin Keller[a], Nada Milisavljević[b], Helmut Süß[a], Marc Acheroy[b]

[a]DLR - German Aerospace Centre, Wessling, Germany
[b]RMA - Royal Military Academy, Brussels, Belgium

## ABSTRACT

Humanitarian demining is a very dangerous, cost and time intensive work, where a lot of effort is usually wasted in inspecting suspected areas that turn out to be mine-free. The main goal of the project SMART* (Space and airborne Mined Area Reduction Tools) is to apply a multisensor approach towards corresponding signature data collection, developing adapted data understanding and data processing tools for improving the efficiency and reliability of level 1 minefield surveys by reducing suspected mined areas. As a result, the time for releasing mine-free areas for civilian use should be shortened.

In this paper, multisensor signature data collected at four mine suspected areas in different parts of Croatia are presented, their information content is discussed, and first results are described.

The multisensor system consists of a multifrequency multipolarisation SAR system (DLR Experimental Synthetic Aperture Radar E-SAR), an optical scanner (Daedalus) and a camera (RMK) for colour infrared aerial views. E-SAR data were acquired in X-, C-, L- and P- bands, the latter two being fully polarimetric interferometric. This provides pieces of independent information, ranging from high spatial resolution (X-band) to very good penetration abilities (P-band), together with possibilities for polarimetric and interferometric analysis. The Daedalus scanner, with 12 channels between visible and thermal infrared, has a very high spatial resolution. For each of the sensors, the applied processing, geocoding and registration is described. The information content is analysed in sense of the capability and reliability in describing conditions inside suspected mined areas, as a first step towards identifying their mine-free parts, with special emphasis set on polarimetric and interferometric information.

**Keywords:** Mine suspected area reduction, SAR, polarimetry, interferometry, multisensor measurements, feature extraction, multispectral signature analysis

## 1. INTRODUCTION

In humanitarian demining, for security reasons, the size of mine suspected areas is widely overestimated at the beginning. With more information available, these suspected areas are reduced to save time and money at the demining process. For the time being, the procedure of mine suspected area reduction consists in an analysis of military reports, like minefield laying records, and field work, such as collection of vegetation cover and interviewing the local population. In that way, the mine suspected area in Croatia was reduced from 13 000 km$^2$ to 1 700 km$^2$ between 1997 and 2001, while it is expected that 170 km$^2$ are really covered by minefields. Demining and fencing activities, reducing the size of mine suspected areas from whole regions to a smaller amount of really dangerous places, and mine risk education of the local population helped to reduce the number of casualties from 340 in the year 1995 to 19 in the year 2001.[1] Additional information from air- or spaceborne sensors could support the decision-making for reducing mine suspected areas, but this possibility is actually rarely used.

E-mail: martin.keller@dlr.de, nada@elec.rma.ac.be
DLR: German Aerospace Centre, Münchner Str. 20, D-82234 Wessling, Germany
RMA: Royal Military Academy, Av. de la Renaissance 30, B-1000 Brussels, Belgium

*SMART is funded by the Information Society Technologies (IST) Programme of the European Community.

From the military mine laying records and demining experience, it is known that many of the used mines have a plastic casing and therefore a poor detectability on the ground by metal sensors. Most mines are buried blast mines, but trip wire fragmentation mines were used too. The most commonly found mines are[2]:

- PMA-1: AP buried blast mine, plastic casing
- PMA-2: AP buried blast mine, plastic casing
- PMA-3: AP buried blast mine, plastic/rubber casing
- PMR-2A: AP tripwire fragmentation mine, iron casing
- PROM-1: AP tripwire fragmentation mine, steel casing
- MRUD: AP tripwire directional fragmentation mine, plastic casing, metal fragments
- TMA-1: AT buried blast mine, plastic casing
- TMA-3: AT buried blast mine, fibre glass casing
- TMA-4: AT buried blast mine, plastic casing
- TMA-5: AT buried blast mine, plastic casing
- TMM-1: AT buried blast mine, sheet steel casing
- TMRP-6: AT buried blast mine, plastic casing

Air- and spaceborne sensors cover large areas in a short time in contrary to information collection from the ground. While experimental radar measurements on uncovered mines and metallic mines in dry sand show, that single mines can be detected under good conditions,[3] a reliable answer about the occurrence and location of small plastic AP mines under vegetation cover is a much more complex task . Due to the experience from earlier projects, it is not expected that single mines can be reliably detected by air- and spaceborne data.[4] Nevertheless, information like vegetation coverage and more abstract features, extracted from air- and spaceborne data and related to minefields, can be used as an additional source of information for the planning of mine clearance. The use of multisensor data that cover the electromagnetic spectrum between visible light and radar, leads to various complementary layers of information about the ground. In order to be helpful to the suspected area reduction process, the provided information has to be reliable, cost-effective, and user-friendly for the end-user, in most times a mine action centre.

The project SMART (Space and airborne Mined Area Reduction Tools) was launched by the EC to help the demining community by developing tools for mine suspected area reduction with use of air- and spaceborne data. Besides RMA and DLR the project partners are: CROMAC (Croatian Mine Action Centre), Croatia; TRASYS, Belgium; ULB (Université Libre de Bruxelles), Belgium; ENST (Ecole Nationale Supérieure des Télécommunications), France; Zeppelin, Germany; RST, Germany; ixl, Germany. The project started in May 2001 and runs for 3 years. In August 2001 a measurement campaign was carried out, data were collected using three sensors in four test areas of $3 \times 4$ km size in different parts of Croatia. A second measurement campaign is planned for summer/autumn 2002, this time using a low and slow flying Zeppelin airship as sensor platform.

The E-SAR (Experimental Synthetic Aperture Radar) collected data in several radar bands while the Daedalus multispectral scanner recorded the electromagnetic spectrum in 12 channels ranging from visible to thermal infrared. The RMK aerial camera was installed on the same aircraft as the Daedalus scanner and collected colour infrared aerial views. E-SAR and Daedalus data are being geocoded and registered to allow for fused data analysis. The RMK aerial views serve as background data source when extreme high spatial resolution is needed.

In an early stage of the demining process, already simple spatial information may be of great value for the mine clearance planning. Information about the status of vegetation, houses or roads can be gathered much faster than from the ground. Later on, such information can be used for change detection, e.g. to find fields that were demined unofficially and are in use now although they are still classified as mine suspected. As the demining process progresses, the tools have to become more sophisticated to be of value for the mine clearance planning. Minefield indicators have to be found that help to divide suspected areas into zones of higher and lower probability of minefields. It is not expected that any feature can be found in air- or spaceborne data that assures that a zone is minefree, the decision to declare an area as not mined can only be reached by

the responsible mine action centre taking into account all available pieces of information. Possible minefield indicators to be found in the recorded data include: unused overgrown paths, disturbed ground, remnants of military objects (dams, trenches, foxholes, former military basecamps), craters, differences in vegetation growth or appearance, natural defense lines (rivers, forest borders).

The following sections give an overview over the data processing and analysis carried out for the project SMART so far. In Section 2 the data acquisition campaign and the processing of the data are described, Section 3 shows examples of the collected image data, Section 4 deals with the analysis of E-SAR and Daedalus data, and finally Section 5 presents plans for our future work in the SMART project.

## 2. DATA COLLECTION

Four test areas that are situated in different parts of Croatia have been chosen for representing different landcover situations. Two of them, Glinska Poljana and Blinjski Kut are fertile valleys surrounded by forested hills in the south of central Croatia near the town of Sisak. Pristeg is a test area in the coastal semiarid area near Zadar while Ceretinci lies in the eastern fertile lowlands near Osijek. Blinjski Kut serves as a validation area for testing the developed tools while the other three test areas are learning sites for mine suspected areas in different regions of the country.

The E-SAR sensor was installed on board a Dornier Do 228 aircraft, the optical multispectral scanner Daedalus and the RMK camera using colour infrared film were mounted on a Cessna Caravan. The weather conditions were ideal (blue sky, no rain, dry soil, few wind).

The following data were recorded:

- E-SAR: X-band ($\lambda = 3.1\,\text{cm}$), vv-polarisation
- E-SAR: C-band ($\lambda = 5.7\,\text{cm}$), vv-polarisation
- E-SAR: L-band ($\lambda = 23\,\text{cm}$), fully polarimetric (hh, hv, vh, vv), repeat pass interferometric analysis is possible with 13 m and 20 m baseline
- E-SAR: P-band ($\lambda = 67\,\text{cm}$), fully polarimetric (hh, hv, vh, vv), repeat pass interferometric analysis is possible with 40 m and 60 m baseline
- Daedalus: 12 channels from visible blue to thermal infrared
- RMK: nearly 400 aerial views

After preprocessing, E-SAR data are available as SLC (single look complex) data in slant range geometry and as geocoded multilook amplitude data for all bands. For L- and P-band additionally an interferometric preprocessing has been carried out, leading to sets of coregistered SLC data of different flight tracks. Daedalus data have been corrected for interrupted scanlines and for perspective dependent sensor sensitivity, calibrated, radiometric normalised, geocoded, and finally the geocoded image stripes have been mosaicked into one image of the test area.

The spatial resolution of the data is:

- E-SAR all data in slant range direction: 2.0 m/2.0 m/2.0 m/4.0 m for X-/C-/L-/P-band
- E-SAR geocoded data in azimuth direction: 1.5 m/1.5 m/2.0 m/4.0 m for X-/C-/L-/P-band
- E-SAR SLC data in azimuth direction: 0.6 m/0.6 m/0.8 m/1.6 m for X-/C-/L-/P-band
- Daedalus: 1 m
- RMK: 3 cm

The data are of high quality, although interferences by other radiation sources are visible in some E-SAR P-band scenes. These interferences are quite common in P-band and the degradation of the data quality was less then we expected from earlier experience.

Two weeks after the flight campaign, a ground truth campaign was carried out by ULB and CROMAC to get better knowledge about the mine situation and the demining process, in addition to existing pieces of information at CROMAC. In all test areas several accessible sites were visited, photos were taken for a better understanding of the airborne data and the demining process was observed.

## 3. IMAGE DATA

In this section we will present image examples of the test area of Glinska Poljana. Since a former front line was running through this region for several years, most parts of the test area are still mine suspected and not used by the local population. In the last years, several secure regions could be handed over to the inhabitants by mine suspected area reduction and mine clearance so that parts of the test area are agriculturally used again, mostly nearby the villages of Glinska Poljana in the north-east and Marinbrod in the south. At the western side one can see the river Glina, followed by mostly mine suspected lowlands and forested hills on the eastern side. In this section E-SAR and Daedalus images of the whole test area will be presented as well as an example of a RMK aerial view.

### 3.1. E-SAR

As image examples of E-SAR data, geocoded amplitude data for X-, C-, L-, and P-band are presented in Figures 1 - 4. For monostatic data collection the hv- and vh-polarisations are identical and can be averaged to one crosspolar channel $xx = \frac{hv+vh}{2}$ so that all independent information is contained in the hh, xx, and vv-polarisations. In L- and P-band the information of the three different polarisations is displayed in rgb-composites (hh: red, xx: green, vv: blue). The contrast in the images increases widely from X-band to P-band. Volume scatterers and rough surfaces reradiate quite homogeneously to all directions and therefore always a certain amount of backscattered energy is received at the sensor. On the other hand, by specular reflection, smooth surfaces scatter most of the energy away from the sensor if the electromagnetic wave does not impinge nearly vertical on the surface.

The penetration ability into a volume increases for longer wavelengths. Since there is only few penetration into the vegetation in X- and C-band, most parts of the objects in the image can be classified as rough surface scatterers after the Rayleigh Criterion. In L-band the same objects divide into volume scatterers like forests and surface scatterers like fields covered by low vegetation. After the Rayleigh Criterion, surfaces become still smoother with respect to the wavelength in P-band and therefore appear very dark compared with other types of scattering. In the forests, the amount of volume scattering decreases with respect to L-band (less backscatter in xx), but an increasing amount of double reflection on the trunks and the ground keeps the backscattered amplitude high (stronger contribution of hh and vv). Therefore forests appear bright but less green in the image. Note that each image has been scaled individually to show all details and therefore a comparison of the absolute brightness between images of different radar bands is not possible.

### 3.2. Daedalus

The appearance of objects in the different Daedalus channels may vary widely, depending on the molecular reflection and absorption characteristics of the matter of the objects. Figure 5 shows an rgb-composite of the red, green and blue Daedalus channels, so it imitates the spectral information that can be seen by the human eye. However the sensitivity of the Daedalus channels to the electromagnetic spectrum is different than of the human eye, thus leading to some colour engraving. In Figure 6 and 8 the information content of three channels in the infrared spectrum (thermal infrared, middle infrared, near infrared) can be observed.

There are several conspicuous stripes in the images running from north to south that come from different orientation angles between sensor, sun, and object, while the aircraft recorded image stripes flying from north to south and back. The effect is minimal when the sun is along the axis of the flight track, the reflectance symmetry to both sides of the tracks then leads to a similar reflectance around the border of two adjacent stripes. Anyhow, the reflectance between the same objects in the middle and at the border of a stripe will be different. This depends on object characteristics and was not compensated during the processing, while the perspective dependent sensor sensitivity only depends on the sensor itself and was eliminated.

### 3.3. RMK

An example for a RMK aerial view is shown in Figure 7. It contains mine suspected and mine free areas that are used for agriculture. Due to the use of a wide angle lens, the decrease of brightness near the borders of the RMK images is quite strong, but since there is some overlap between different RMK images, there is always an image that shows the place of interest bright enough for analysis.

## 4. DATA ANALYSIS

The analysis of first data started in December 2001, after the export permission was granted by Croatian authorities and data could be shipped to Germany and processed. By now, some first steps towards the final goal of mine suspected area reduction have been done, but there is still a lot of ongoing and planned work to be carried out.

### 4.1. E-SAR

We focussed our work on E-SAR data on L- and P-band SLC data, which can be used for polarimetric and interferometric analysis. A Pauli decomposition[5] has been calculated in order to get knowledge about the type of scattering. The Pauli decomposition separates all scatterers into three basic types by simple transformations of the complex scattering elements for each pixel:

- Scatterers with an odd number of reflections like surfaces (one bounce) or the corner reflector (three bounces)
- Scatterers with an even number of reflections like at trunks and the ground or at walls and the ground
- Scatterers with a crosspolar response (multiple reflections in volume scatterers like forests or corn fields, or scattering of a dihedral tilted by 45° to the line of sight)

The scattering matrix can be decomposed into Pauli matrices by

$$[S] = \begin{bmatrix} S_{hh} & S_{hv} \\ S_{vh} & S_{vv} \end{bmatrix} = \begin{bmatrix} a+b & c-id \\ c+id & a-b \end{bmatrix} = a \begin{bmatrix} 1 & 0 \\ 0 & 1 \end{bmatrix} + b \begin{bmatrix} 1 & 0 \\ 0 & -1 \end{bmatrix} + c \begin{bmatrix} 0 & 1 \\ 1 & 0 \end{bmatrix} + d \begin{bmatrix} 0 & -i \\ i & 0 \end{bmatrix} \quad . \quad (1)$$

With the set of Pauli matrices

$$\psi_P : \quad \sqrt{2} \begin{bmatrix} 1 & 0 \\ 0 & 1 \end{bmatrix}, \sqrt{2} \begin{bmatrix} 1 & 0 \\ 0 & -1 \end{bmatrix}, \sqrt{2} \begin{bmatrix} 0 & 1 \\ 1 & 0 \end{bmatrix}, \sqrt{2} \begin{bmatrix} 0 & -i \\ i & 0 \end{bmatrix} \quad , \quad (2)$$

the Pauli target vectors can be calculated by

$$\vec{k}_P = \frac{1}{2} \operatorname{trace}([S]\,[\psi_{X_P}]) = \frac{1}{\sqrt{2}} \begin{bmatrix} S_{hh} + S_{vv} \\ S_{hh} - S_{vv} \\ S_{hv} + S_{vh} \\ i(S_{hv} - S_{vh}) \end{bmatrix} \quad . \quad (3)$$

In the monostatic case $S_{hv} = S_{vh} = S_{xx}$ and the last element of the Pauli target vector gets zero so here we get

$$\vec{k}_P = \frac{1}{2} \operatorname{trace}([S]\,[\psi_{X_P}]) = \frac{1}{\sqrt{2}} \begin{bmatrix} S_{hh} + S_{vv} \\ S_{hh} - S_{vv} \\ 2S_{xx} \end{bmatrix} \quad . \quad (4)$$

The first Pauli matrix describes a zero degree phase shift between $S_{hh}$ and $S_{vv}$ which can be achieved by an odd number of specular reflections, while the second Pauli matrix introduces a 180° phase shift which has its physical meaning in an even number of reflections. The rotation dependence about the line of sight of an even bounce scattering is described by the third Pauli matrix that corresponds to the response of a dihedral, tilted by 45° about the line of sight. The above is valid for the backscatter alignment convention, describing a wave in an antenna fixed coordinate system. In nature, multiple scattering in volumes leads to arbitrary phase shifts and therefore to a substantial contribution of crosspolarised backscatter.

Figures 9-12 show the four test areas after Pauli decomposition in L- and P-band (red: odd bounce, green: volume scatterers and 45° tilted double bounce, blue: double bounce). The images are shown in slant range geometry, therefore distances in near range (lower part of the image) are compressed. It can be observed that in L-band there is a stronger contribution of volume scattering than in P-band (the images appear more green). Due to the good penetration abilities of P-band in the forests, the double bounce contribution from trunks and

the ground increases and forests appear more red. There is a visible trend from blue in near range to red in far range, resulting from the dependence of the strength of a backscattered single bounce reflection on the incidence angle. For an ideal specular single bounce reflection at a perfectly smooth surface, only for a vertical incidence a very strong signal could be received while for all other directions all the energy would be scattered away from the sensor. Luckily, nature is not that perfect, and therefore the single bounce contribution can be observed for all incidence angles even though the signal gets weaker in far range.

The pioneer vegetation of the mine suspected fields does not have much volume or double bounce scattering contribution. Therefore, by the use of Pauli decomposed data, the suspected fields are separable from most cultivated fields, except those with no or few vegetation cover like meadows or bare fields. Structures inside the mine suspected areas can be found and it has to be analysed if they originate from vegetation, soil, soil moisture or human influence that may lead to an indication for minefields.

Interferograms were calculated for all test areas with baselines of 13 m in L-band and 40 m in P-band. From an interferogram the interferometric coherence can be extracted which is a measure of the amount of phase noise in an interferometric pair of SLC data.[6] It is defined as the normalised complex cross-correlation between these two data sets:

$$\gamma = \frac{|\langle \mathrm{SLC}_1 \times \mathrm{SLC}_2^* \rangle|}{\sqrt{\langle \mathrm{SLC}_1 \times \mathrm{SLC}_1^* \rangle \langle \mathrm{SLC}_2 \times \mathrm{SLC}_2^* \rangle}} \tag{5}$$

Theoretically, the similarity of the data sets should be described by the expectation values, but because only one interferogram is available, the expectation value has to be replaced by spatial averaging. A coherence value of $\gamma = 1$ means, that the interferometric phase at all pixels, which are taken into account is the same. For very low coherences ($\gamma \to 0$), the different phase values are totally random, so only noise remains. The images in Figures 13-16 show the coherences for interferometric data in L- and P-band for all test areas. Usually coherence values are scaled from black ($\gamma = 0$) to white ($\gamma = 1$). Here the three different basic coherences hhhh (between the two horizontal polarisations), xxxx (between the crosspolar elements), and vvvv (between the vertical polarisations) have been combined to rgb-images. White parts show high coherences in all polarisations, dark parts are strongly decorrelated, and coloured parts have a strong dependence of the coherence on the polarisation. As an example, surface scatterers have a low backscatter in xx, so here the influence of the noise gets strong enough to decorrelate the interferometric phases, even if the scatterers did not change at all. Those areas often have a high coherence in the copolar channels (bright red and blue) but a low coherence in the crosspolar components (dark green) and therefore appear violet in the image.

The forests in the test areas Glinska Poljana, Blinjski Kut and Ceretinci in Figures 13, 14, and 16 show a strong decrease in coherence due to volume decorrelation (decrease of coherence by the contribution of non-identical parts of the vertical vegetation structure to the values of the same pixels in the interferometric pair of data). On the contrary, the low macchia at the test site Pristeg in Figure 15, that also sends back substantial crosspolar backscatter has a very high coherence.

In repeat pass interferometric data, another important source of loss of coherence is the temporal decorrelation due to the change of scatterer properties (e.g. dry soil at the first pass, wet at the second) or positions (e.g. movement of trees because of wind) in between the two recordings. In our case the time offset was less than one hour in stable weather conditions and temporal decorrelation did not decrease significantly the coherence as can be seen in the high values for the agriculturally used areas at all test sites and the macchia at Pristeg.

Very often, the suspected fields show a medium to low crosspolar coherence in P-band, mainly due to a low signal to noise level for crosspolar backscatter in surface scattering. In P-band, due to the Rayleigh Criterion, the surfaces have much smoother characteristics than in L-band, where often suspected areas with very high coherence can be found that cannot be separated from crop. The coherence information is much more robust to variations of the incidence angle than the backscattered amplitudes from surfaces, and therefore P-band coherence can be used very well as a tool to separate unused fields from most of the agricultural used areas. Figure 17 shows different types of landuse: crop, bare fields, and in the surrounding still mine suspected area. The crop has a high coherence (bright), the bare fields a low coherence for all polarisations (dark) while the suspected fields have low coherence only at the crosspolar component (violet). However a classification will not

be unequivocal, some agricultural used fields have similar coherence properties than the pioneer vegetation of suspected fields, and have to be separated by other means.

### 4.2. Daedalus

Multispectral remote sensing relies on the fact that different materials or types of landcover reflect and absorb solar radiation in a different way at various wavelengths. In other words, any material or type of landcover has its unique multispectral signature, that can be represented by a plot of the fraction of reflected radiation as a function of the incident wavelength. For example, clear water has a low reflectance in general, but it has its maximum at the blue part of the spectrum and decreases with the increasing wavelength. The reflectance of bare soil, on the contrary, increases monotonically with the wavelength. In case of vegetation, its reflectance has minima in the blue and in the red region of the spectrum, while it has a peak in the green region. As the wavelength increases towards the near-infrared region, the reflectance significantly increases and becomes much higher than in the visible region. Besides these general tendencies of water, soil and vegetation, there are differences in the exact shape of the reflectance spectrum (or spectral signature) between different types of the same class. This means, e.g., that the exact shape of the bare soil signature depends on the type of soil, its composition, moisture, etc. These examples indicate the main idea of our work with the Daedalus data: the use of the shape of the multispectral signature for landcover classification. Thus, we analyse the multispectral signatures and then assign pixels to classes based on similar signatures.

There are two possibilities for multispectral classification. In supervised classification, classes are associated with known features on the ground, while in unsupervised classification, the pixels are analysed in an automatic way and divided in spectrally distinct classes (accumulations of points in a multidimensional feature space). The latter type of classification is used when the knowledge about the data is low before classification, and the output is provided to the image analyst, who should give meaning to the resulting classes.

On the one hand, we do not have a reliable information on the minefield indicators at this stage of our project (actually, determining the useful minefield indicators is one of the goals of the project). On the other hand, we should be cautious and avoid any misclassification which could be caused by the human interaction and which, in this context, can have dangerous consequences. Therefore, our plan is to proceed in the following way:

- firstly, to apply an unsupervised classification and by that obtain classes of different landcover;
- using the ground-truth information, we attach meaning to some typical and wide-spread landcover classes (e.g. grass, forest, cornfield);
- the remaining, unlabeled regions might be related to some landcover anomalies, hence they are possibly dangerous and should be further analysed in detail.

At this moment, the first step given above is finished, and we are analysing the ground-truth information towards extracting the regions of known landcover. Note that this step, as well as the next one, has to proceed very carefully, hence slowly, in order not to miss, discard or misclassify any mined area. The fact that the mine density in the affected regions of Croatia is often very low further justifies the need of being extremely cautious.

While applying this unsupervised classification, we take advantage of another fact related to the multispectral signature analysis, namely the information provided by comparing the reflectance in the red region ($r$) and in the near-infrared region ($n$), known as vegetation index. The normalised difference vegetation index *NDVI* is defined by

$$NDVI = \frac{n - r}{n + r} \tag{6}$$

and is:

- negative for water and snow;
- close to 0 for rocks and bare soil;
- between 0 and $\frac{1}{3}$ for lower vegetation;
- increases above $\frac{1}{3}$ with the density and vitality of the plant canopy (e.g. for forests and fresh vegetation).

Neither water nor forests are potential minefield indicators. Since there is not much fresh biomass in the several year old pioneer vegetation of the mine suspected fields, we can mask areas with vegetation indices of $NDVI < 0$ and $NDVI > \frac{1}{3}$ before applying a landcover classification.

To summarise, our unsupervised classification proceeds as follows. The 12 channels of the Daedalus data are analysed pixel per pixel. A first analysed pixel creates a first class, and its multispectral signature (so its values in the 12 channels, $p_{1\,1}$, $p_{1\,2}$, ..., $p_{1\,12}$) is stored as the representative of that class, $c_{1\,1}$, $c_{1\,2}$, ..., $c_{1\,12}$. The next pixel, having $p_{2\,1}$, $p_{2\,2}$, ..., $p_{2\,12}$ as values in the 12 channels is compared with the representative of the first class by finding their distance $t$, as

$$t = \frac{1}{12}\sqrt{\sum_{i=1}^{12}(p_{2\,i} - c_{1\,i})^2} \tag{7}$$

If $t$ is lower than or equal to a preset tolerance, $k$, the analysed pixel is grouped in the first class, and the representative multispectral signature of that class is updated, i.e. replaced by averaging the signature of the new found pixel and the existing pixel in the class. If $t > k$, the analysed pixel creates a new class, and its values initialise the multispectral representative of that class. A separate rejection class is formed for all pixels having $NDVI < 0$ or $NDVI > \frac{1}{3}$. The procedure continues in a similar way, so that each pixel signature is compared with all existing classes. The pixel is always grouped to the class having the minimum distance $t$ or, if $t > k$, creates a new class. When all pixels are analysed, we get a first output of the unsupervised classification, together with the final multispectral signature representative for each of the classes. Here we have two possibilities. Our method can either end here, or go on for a new iteration, starting with the results of the last iteration as a priori classes. Namely, since the process of finding the multispectral signatures of the classes in the first iteration consists of updating the representatives of each class every time a new member of the class is found, we can expect misclassifications for pixels belonging to similar types of vegetation. Once we have fixed the representatives, we can use them to reclassify the pixels and, hopefully, correct most, if not all, misclassifications. In addition, in this way, a strong influence of the choice of the preset tolerance, $k$, affecting the number of classes, is diminished to some extent.

We illustrate the above proposed method for the region shown in Figure 18 and 19. Results of the method for $k = 22$ (10 resulting classes) and $k = 19$ (20 classes) are shown in Figure 22. By increasing the number of classes, both noise (single pixels grouped to other classes than their surrounding) and the level of details increase, where the latter could lead to identifying possible landcover anomalies. Although the classified data are relatively noisy in this stage of our work, we decided not to smooth the image in order to preserve potential minefield indicators.

### 4.3. Combined Analysis

In Figure 18 and 19 an area of 500 m by 500 m in the Glinska Poljana test site is displayed, containing mostly mine suspected fields. E-SAR images are in slant range geometry while Daedalus images are geocoded. Both E-SAR and Daedalus data show many structures which sometimes, but not always, coincide. A simple explanation could be, that the similar structures arise from differences in the vegetation cover, which changes the reflection in the visible and infrared light, as well as the scattering properties for longer wavelengths. The differences would then come from sources which are seen only by one sensor. Either the cause would lie below the vegetation surface and be detectable only by E-SAR, or they would have to come from colour differences of the vegetation without changing the radar scattering properties. Although this explanation sounds reasonable, it has to be further analysed.

An example of a rgb-composite of channels from different sensors is shown in Figure 21. It shows the village of Marinbrod in the Glinska Poljana test area. At the right side of the image, demining activities can be observed. The red and green colours show channels 11 and 9 of the Daedalus data, while a geocoded E-SAR L-band vv-polarisation image is shown in blue. Due to the imaging geometry of side looking SAR sensors, elevated objects like trees or roofs are shifted to the sensor (layover effect). On the other hand, in Daedalus images the position of elevated objects is shifted away from the sensor in off-nadir regions. This results from using a DEM for geocoding that represents the topography, but not the surface cover like forests or houses. In

the worst case, elevated objects are shifted to opposite directions, and E-SAR and Daedalus geocoded images do not fit for them. On the other hand, if both errors show to the same direction, it might not be visible in the image. If an object is situated at the surface of the DEM, it is mapped to the same, correctly geocoded place in the image by both sensors. Since we are interested in the ground and the low part of the vegetation cover, the mapping precision will be sufficient for our purposes. The field and the hedge in the central part of the image show backscatter in the E-SAR image, which matches well with the Daedalus imagery. The geocoding error $x$ at an elevated object of the height $h$ depends on the look angle $\varphi$ and is calculated by $x = \frac{h}{\tan\varphi}$ for E-SAR data. It results to $x = 1.88 \cdot h$ in near range and $x = 0.70 \cdot h$ in far range. For Daedalus data the geocoding error is $x = h \tan\varphi$, so there is no error at the nadir, while for far off-nadir objects it can be as high as $x = h$. The height $h$ represents the objects surface for Daedalus data, while due to penetration, $h$ is less for volume scatterers like trees in E-SAR data.

## 5. CONCLUSIONS AND FURTHER WORK

First results of the analysis of data, recorded for the project SMART, are discussed. Geocoded E-SAR and Daedalus data, E-SAR SLC Pauli decomposition results and interferometric coherence images, as well as a multispectral landcover classification of Daedalus data are presented and discussed. The analysis of the interferometric SAR coherence and the multispectral landcover classification are most promising for separating mine suspected fields from other vegetation. Inside a mine suspected area, different structures can be observed in multispectral and SAR data. The knowledge about the physical sources of these structures will be a key point in our further work. We plan to continue with polarimetric and interferometric SAR data analysis, using decomposition and classification techniques.[7–9] Results of work on slant range SLC data will be geocoded for fusing them with Daedalus data. Landcover classification from Daedalus data will be further improved. We expect that the classification of fused E-SAR/Daedalus data will result in good separation of classes due to less correlated input. The developed tools for information extraction will be implemented in a GIS and provided to an image interpreter at the Croatian Mine Action Centre for further reduction of mine suspected areas.

## ACKNOWLEDGMENTS

This work was carried out inside the project SMART, funded by the Information Society Technologies (IST) Programme of the European Community. The authors thank project partners and colleagues from DLR and RMA for invaluable discussions and suggestions.

## REFERENCES

1. Croatian Mine Action Centre, Sisak, Croatia, *Four Years of CROMAC's Operations*, Feb. 2002.
2. M. Bajić, "Redefinition the Objectives of the Airborne Remote Sensing for Humanitarian Demining: Exponential Growth of the Remediated Area," in *Workshop on the needs of airborne and spaceborne data for minefield survey*, (Ispra, Italy), 2000.
3. T. Grosch, C. Lee, and E. Adams, "Detection of Surface and Buried Mines with a UHF Airborne SAR," in *SPIE Proceedings*, **2496**, pp. 110–120, (Orlando, Florida), 1995.
4. International Institute for Aerospace Survey and Earth Sciences (ITC), *Airborne Minefield Detection: Pilot Project - Final Report*, 1999.
5. S. Cloude, "Polarisation Effects in Low Order Multiple Scattering," in *Proceedings of the 2nd International Workshop on Radar Polarimetry*, pp. 79–95, (Nantes, France), 1992.
6. K. P. Papathanassiou, *Polarimetric SAR Interferometry*. PhD thesis, Technical University Graz, Jan. 1999.
7. S. Cloude and E. Pottier, "An Entropy Based Classification Scheme for Land Applications of Polarimetric SAR," *IEEE Transactions on Geoscience and Remote Sensing* **35**, pp. 68–78, Jan. 1997.
8. E. Krogager and Z. Czyż, "Properties of the Sphere, Diplane, Helix Decomposition," in *Proceedings of the 3rd International Workshop on Radar Polarimetry (JIPR '95)*, pp. 106–114, (Nantes, France), 1995.
9. L. Ferro-Famil, E. Pottier, and J.-S. Lee, "Unsupervised Classification of Multifrequency and Fully Polarimetric SAR Images Based on the H/A/Alpha-Wishart Classifier," *IEEE Transactions on Geoscience and Remote Sensing* **39**, pp. 2332–2342, Nov. 2001.

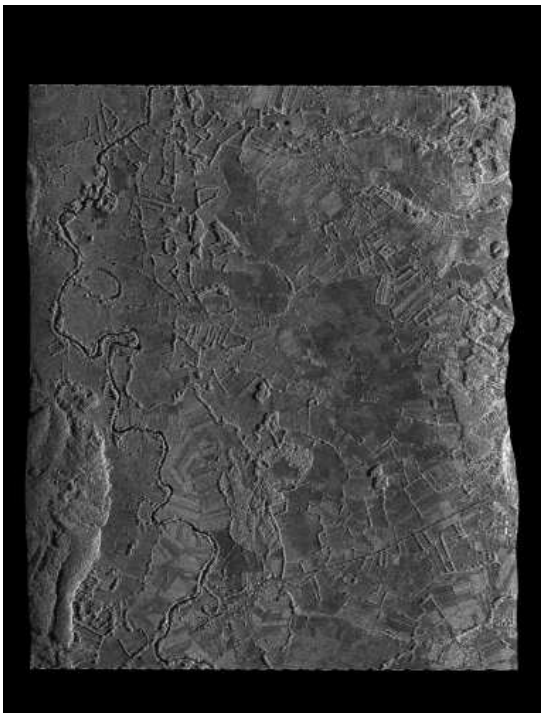

**Figure 1.** Geocoded E-SAR X-band vv-polarisation image of Glinska Poljana

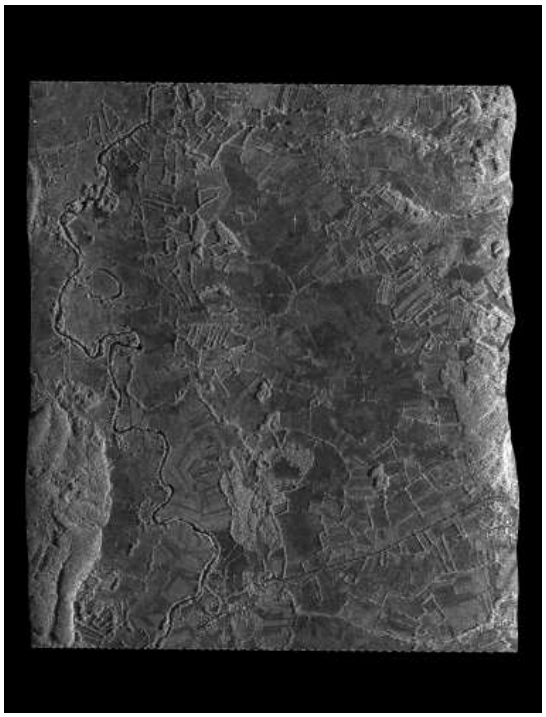

**Figure 2.** Geocoded E-SAR C-band vv-polarisation image of Glinska Poljana

**Figure 3.** RGB-composite of geocoded E-SAR L-band images of Glinska Poljana (r,g,b = Lhh, Lhv, Lvv)

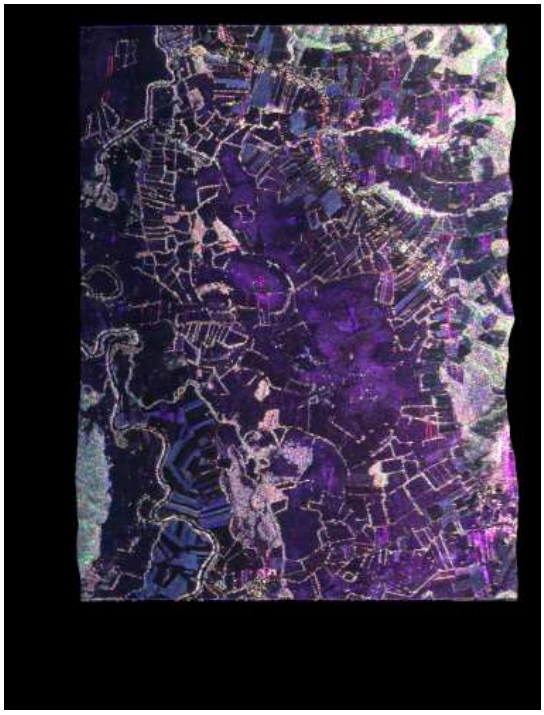

**Figure 4.** RGB-composite of geocoded E-SAR P-band images of Glinska Poljana (r,g,b = Phh, Phv, Pvv)

**Figure 5.** RGB-composite of geocoded Daedalus channels of Glinska Poljana. r,g,b = ch5 (red), ch3 (green), ch2(blue)

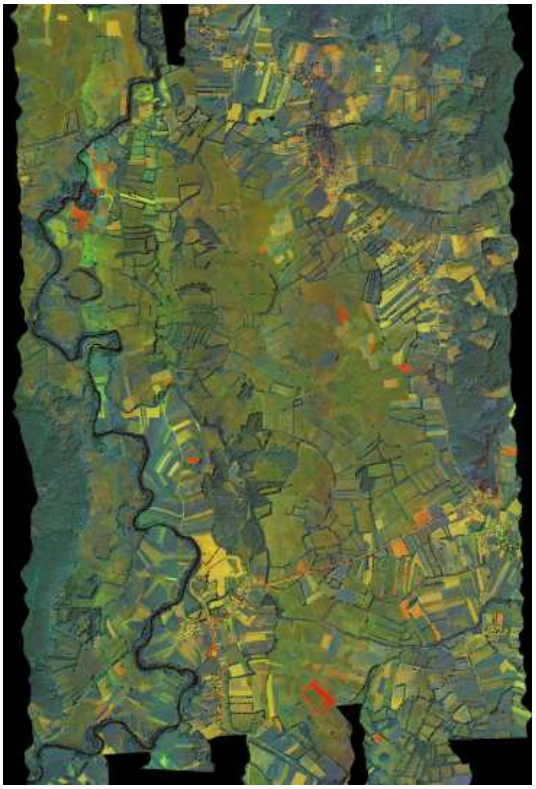

**Figure 6.** RGB-composite of geocoded Daedalus channels of Glinska Poljana. r,g,b = ch11 (thermal infrared, contrast enhanced), ch9 (middle infrared), ch7(near infrared)

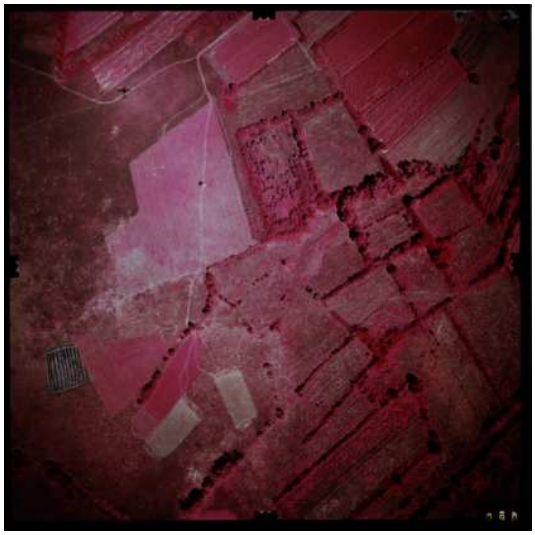

**Figure 7.** Colour infrared aerial view at Glinska Poljana. r,g,b = near infrared, red, green

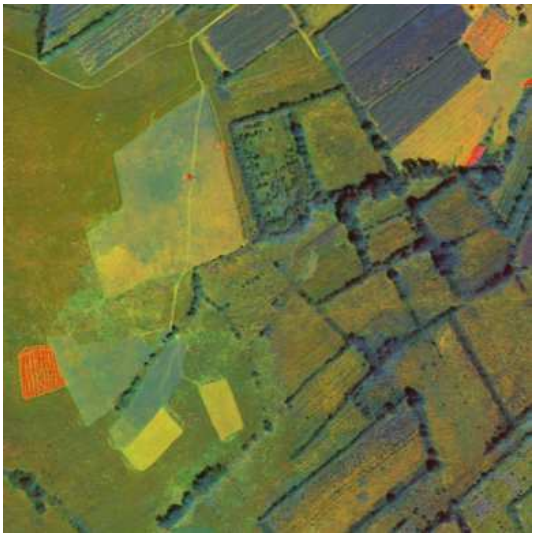

**Figure 8.** Zoom to the corner reflector area and suspected fields. RGB-composite of geocoded Daedalus channels of Glinska Poljana. r,g,b = ch11 (thermal infrared, contrast enhanced), ch9 (middle infrared), ch7(near infrared)

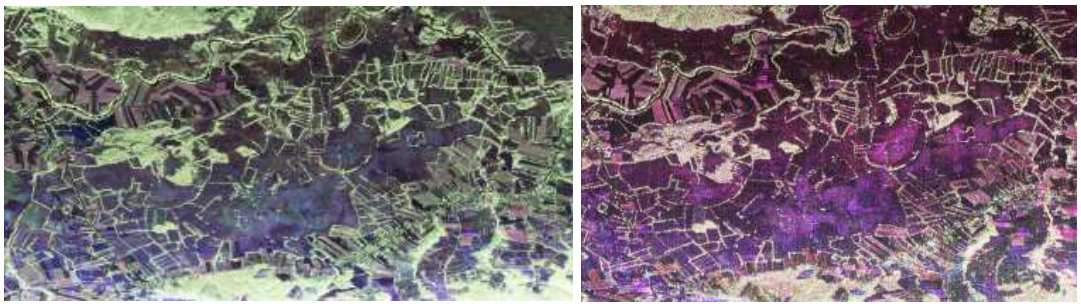

**Figure 9.** E-SAR L- and P-band images of Glinska Poljana in Pauli decomposition.
red: even number of reflections, green: volume scattering and 45° tilted double bounce, blue: odd number of reflections

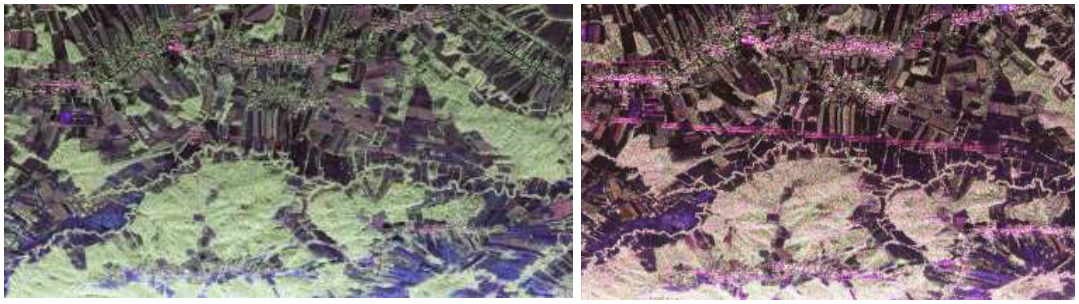

**Figure 10.** E-SAR L- and P-band images of Blinjski Kut in Pauli decomposition.
red: even number of reflections, green: volume scattering and 45° tilted double bounce, blue: odd number of reflections

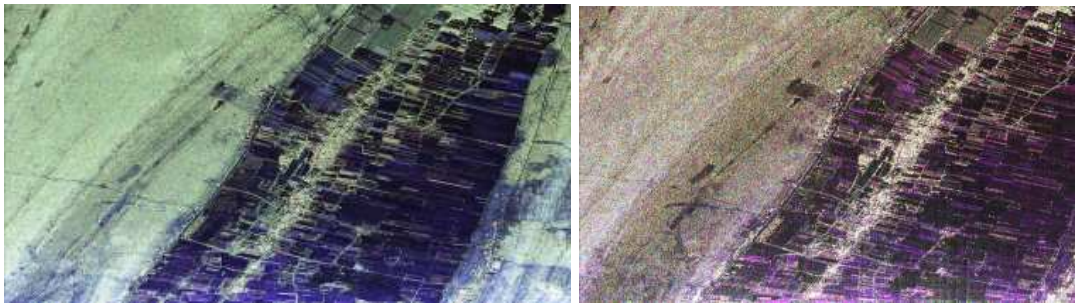

**Figure 11.** E-SAR L- and P-band images of Pristeg in Pauli decomposition.
red: even number of reflections, green: volume scattering and 45° tilted double bounce, blue: odd number of reflections

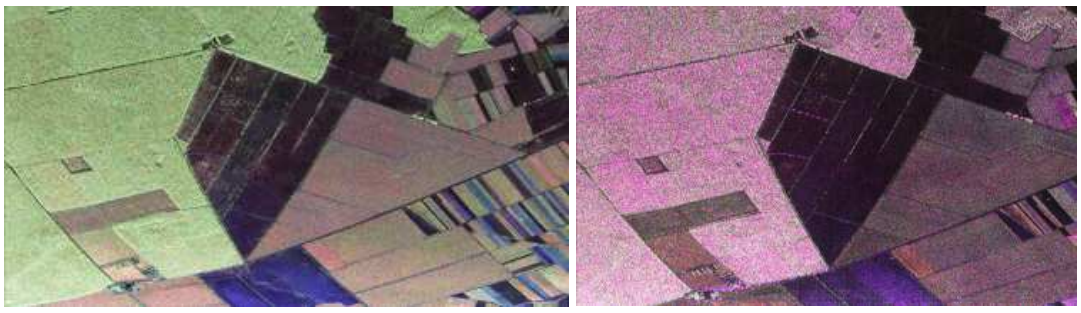

**Figure 12.** E-SAR L- and P-band images of Ceretinci in Pauli decomposition.
red: even number of reflections, green: volume scattering and 45° tilted double bounce, blue: odd number of reflections

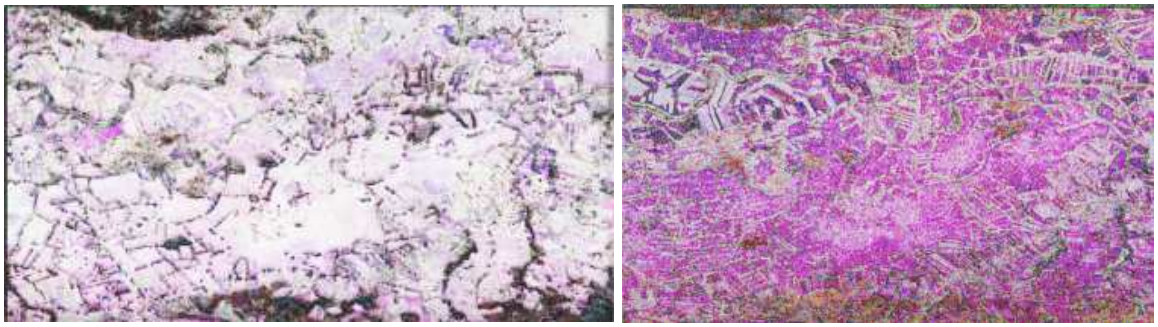

**Figure 13.** E-SAR L- and P-band interferometric coherence at Glinska Poljana.
red: hhhh-coherence, green: xxxx-coherence, blue: vvvv-coherence

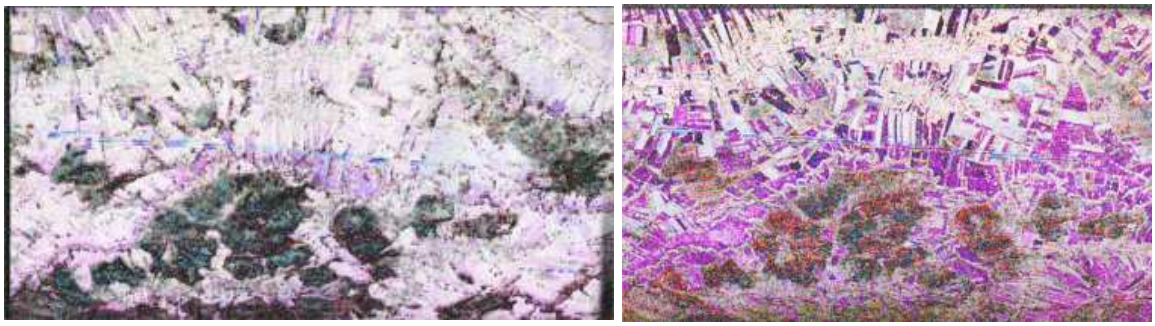

**Figure 14.** E-SAR L- and P-band interferometric coherence at Blinjski Kut.
red: hhhh-coherence, green: xxxx-coherence, blue: vvvv-coherence

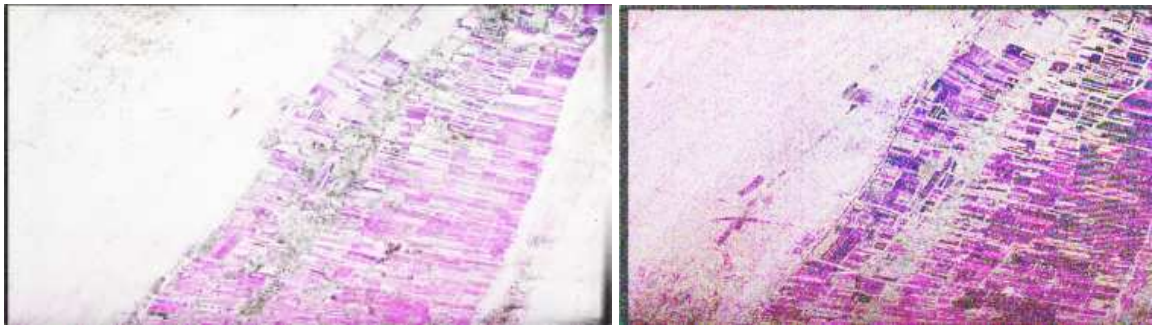

**Figure 15.** E-SAR L- and P-band interferometric coherence at Pristeg.
red: hhhh-coherence, green: xxxx-coherence, blue: vvvv-coherence

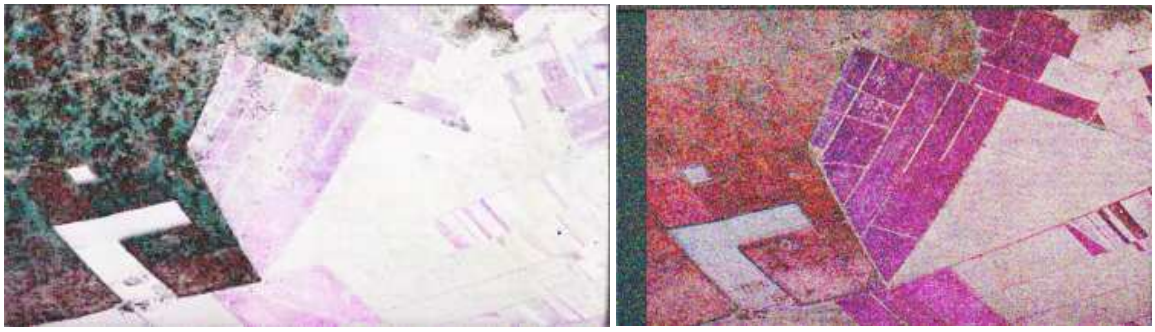

**Figure 16.** E-SAR L- and P-band interferometric coherence at Ceretinci.
red: hhhh-coherence, green: xxxx-coherence, blue: vvvv-coherence

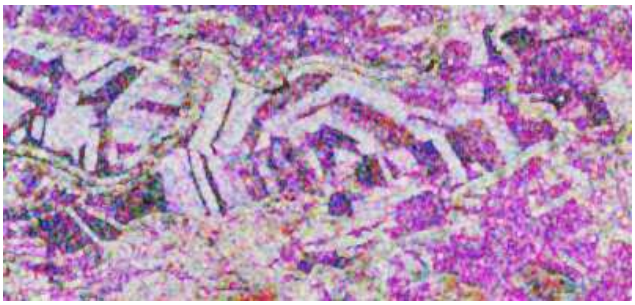

**Figure 17.** E-SAR P-band interferometric coherence of an agricultural used area and surrounding mine suspected fields in the Glinska Poljana test site. red: hhhh-coherence, green: xxxx-coherence, blue: vvvv-coherence

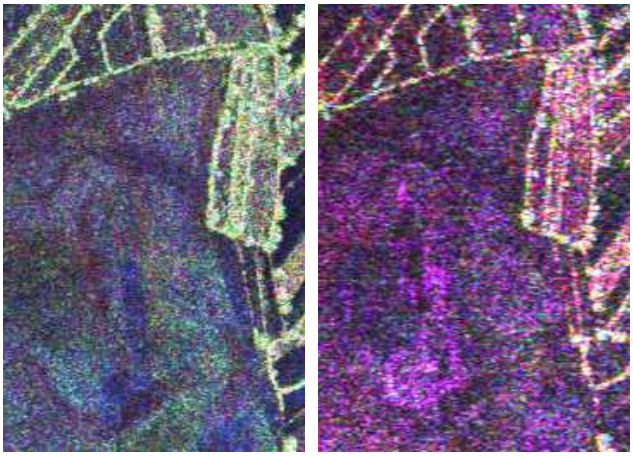

**Figure 18.** E-SAR L- and P-band SLC slant range images of a mine suspected area at Glinska Poljana in Pauli decomposition. red: even number of reflections, green: volume scattering and 45° tilted double bounce, blue: odd number of reflections

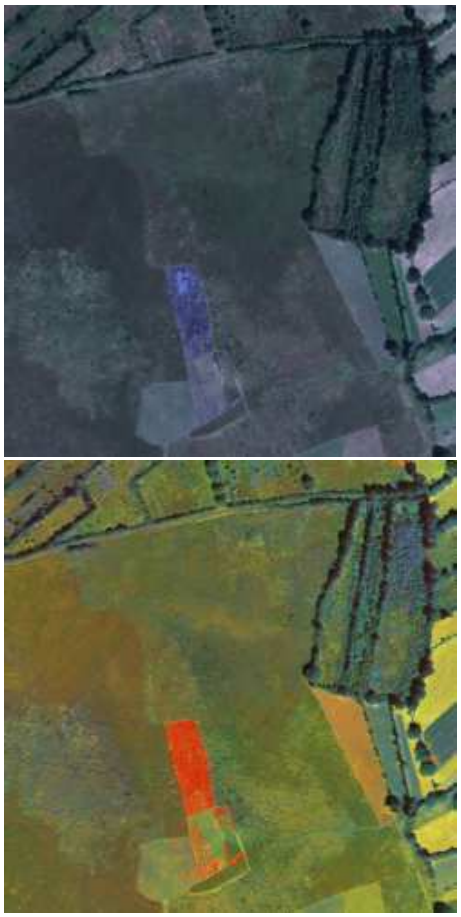

**Figure 19.** Daedalus geocoded images of a mine suspected area at Glinska Poljana.
First image: r,g,b = ch5,ch3,ch2 (visible)
Second image: r,g,b = ch11,ch9,ch7 (infrared)

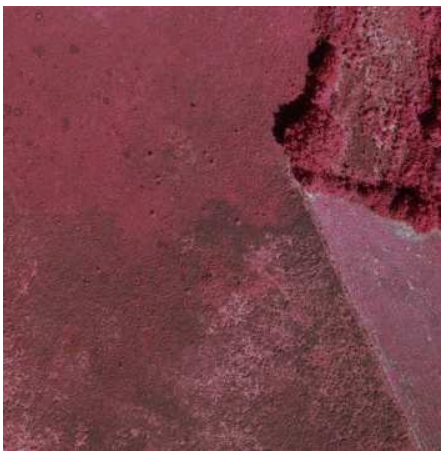

**Figure 20.** RMK image of a mine suspected area at Glinska Poljana.

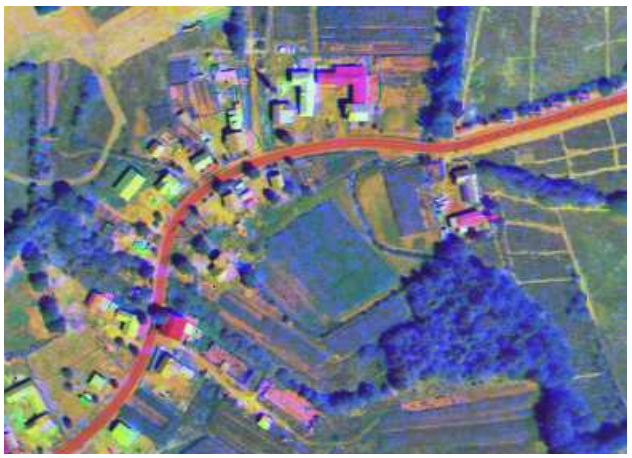

**Figure 21.** RGB composite of Daedalus and E-SAR geocoded data, village of Marinbrod.
r,g,b: Daedalus ch11, ch9, E-SAR Lvv

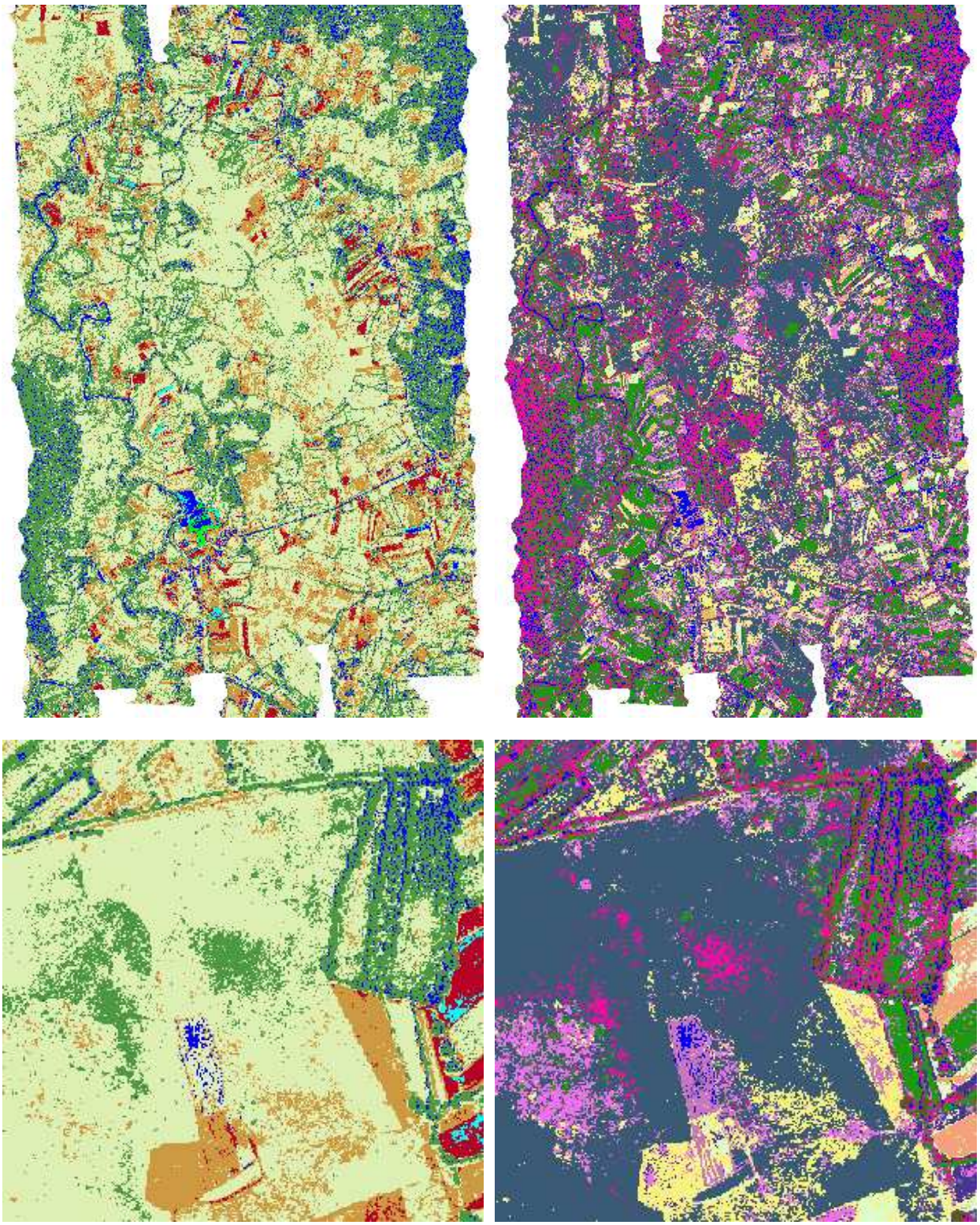

**Figure 22.** Preliminary results of an unsupervised classification of Daedalus data for the test area Glinska Poljana: 10 classes (left), 20 classes (right). The lower images show the same mine suspected area as Fig. 19